Cognitive modulation of interacting corollary discharges in the visual cortex

Mohammad Abdolrahmani[1*], Dmitry R. Lyamzin[1*], Ryo Aoki[1], Andrea Benucci[1]

[1] RIKEN Center for Brain Science, Wako-shi, 351-0198 Saitama, Japan

* These authors contributed to the work with equal effort

Abstract

Perception is an active process involving continuous interactions with the environment. During such interactions neural signals called corollary discharges (CDs) propagate across multiple brain regions informing the animal whether itself or the world is moving. How the interactions between concurrent CDs affect the large-scale network dynamics, and in turn help shape sensory perception is currently unknown. We focused on the effect of saccadic and body-movement CDs on a network of visual cortical areas in adult mice. CDs alone had large amplitudes, 3-4 times larger than visual responses, and could be dynamically described as standing waves. They spread broadly, with peak activations in the medial and anterior parts of the dorsal visual stream. Inhibition mirrored the wave-like dynamics of excitation, suggesting these networks remained E/I balanced. CD waves superimposed sub-linearly and asymmetrically: the suppression was larger if a saccade followed a body movement than in the reverse order. These rules depended on the animal's cognitive state: when the animal was most engaged in a visual discrimination task, cortical states had large variability accompanied by increased reliability in sensory processing and a smaller non-linearity. Modeling results suggest these states permit independent encoding of CDs and sensory signals and efficient read-out by downstream networks for improved visual perception. In summary, our results highlight a novel cognitive-dependent arithmetic for the interaction of non-visual signals that dominate the activity of occipital cortical networks during goal-oriented behaviors. These findings provide an experimental and theoretical foundation for the study of active visual perception in ethological conditions.

Introduction

Corollary discharges (CDs) are copies of motor commands that do not themselves produce body movements, but inform brain regions on whether the animal or the world is moving[1-4]. These signals are found ubiquitously in the animal kingdom[2] and it is increasingly understood they profoundly impact the dynamics of several brain regions, affecting sensory perception as well[5-8]. During ethological behaviors multiple CDs concurrently propagate across neural networks[1]. However in traditional approaches CDs have been either isolated one at a time for experimental convenience or labelled as uncontrolled variability and abolished with anesthetized preparations or behavioral paradigms that minimize motor components. Accordingly, how CDs interact with each other and how these interactions affect sensory perception during goal-directed behaviors is currently unknown.

We addressed these questions in the visual cortex of awake mice, which has served as a model system for two very well-studied CDs, those for saccadic eye movements[9-14] and for body movements[15-20]. We first characterized the large-scale dynamics of the CDs analyzed individually or when interacting with each other and with visual signals. Then we examined the cognitive dependence of the found properties and their relevance to perception by studying the animals' behavior in a visual discrimination task.

Results

Mice (n=15) were trained in a two-alternative forced choice (2AFC) orientation discrimination task (Fig. 1a,b, Extended Data Fig. 1a) with automated setups featuring self head-fixation[21]. Head-fixed mice made frequent voluntary saccadic eye movements mostly in the nasal-temporal direction[22] (Fig. 1c, Extended Data Fig. 1d, Supp. Video 1) and preferentially after the stimulus presentation (in the open-loop period, OL, Fig. 1a,d), possibly reflecting a task-related exploration of the visual stimuli. This saccadic pattern emerged with training, with naïve animals making significantly fewer exploratory eye movements despite being shown the same visual stimuli – more salient given their novelty (Extended Data Fig. 1b). Animals reported their choice by rotating a wheel with their front paws[23] (Fig. 1a,b). Wheel rotations – from hereafter denoted 'body movement' – were associated with more general movements of the trunk, tail, snout, whiskers, etc., (Supp. Video 2).

During behavior we imaged responses from excitatory neurons in a large network of visual cortical areas (n=10 mice, Fig. 1e, Extended Data Fig. 1c, Methods). Notably, responses to isolated saccades were about four times larger than contrast responses (Fig. 1f), even in the V1 retinotopic location of the stimulus (Fig. 1f-g). Saccades strongly activated medial V1 and the medial part of the dorsal visual stream (areas PM, AM, A, Fig. 1g, Extended Data Fig. 2a,b,g) – regions implicated in the *magnocellular hypothesis* of saccadic suppression[14,24] – anterior visual-parietal areas[25] (Extended Data Fig. 2i,j) and partially-imaged somatosensory areas[26]. After about half a second of transient increase, the response was followed by a delayed suppression below baseline activity (Fig. 1f). The overall dynamics could be described in terms of a global spatial pattern whose amplitude was modulated over time, i.e. a standing wave of activity (Extended Data Fig. 3a, Methods). Deviations from the wave dynamics (residuals of a singular-value decomposition, Methods) revealed a small but significant response in motion sensitive areas[27] (i.e. RL, AL and LM, Extended Data Fig. 3c) with peak amplitude about 1.4 seconds after the onset of the saccade, possibly linked to a reafferent retinal signal, i.e. a sensory input induced by the eye movements.

However, reafference was not a significant contributor to the overall response pattern. Indeed, the onset of neural activity preceded the onset of saccades by 110ms (-110±20ms, s.e.), with the spatial profile of the activation already matching that of the post-saccadic response (Extended Data Fig. 2c). Nasal or temporal saccadic eye movements did not produce significantly different activations (Extended Data Fig. 2d), as it should be expected by reafferent signals[1,2]. Furthermore, in experiments where we jittered the stimuli on the screen with displacement vectors and velocities drawn from the distribution of actual saccades (simulated saccades[28], Extended Data Fig. 1e, Methods), responses had smaller amplitudes than saccadic ones and were localized in motion-sensitive areas[27] (Fig. 1f,g). Finally, saccadic responses in the absence of contrast stimuli (Methods) and of behavioral task ("blanks") were comparable to those evoked in the presence of contrast stimuli, although the delayed suppression was significantly reduced (Extended Data Fig. 4a-c).

The second corollary discharge we examined was related to body movements[16], also typically occurring after the stimulus onset (Fig. 1d). Consistent with studies on locomotion[5,15], body movements elicited large-amplitude responses, about three times larger than responses to visual stimuli (Fig. 1f,g). They localized in medial V1 and dorsal stream areas (Fig. 1g), such as the posterior parietal cortex (A, anterior-RL, and AM[25]), and the hind-paw somatosensory areas[26]. Similar to saccades, responses emerged before the initiation of the wheel rotation (-237±31ms, s.e.; n=10; Extended Data Fig. 2c) reflecting either a pre-motor preparatory component[8,19,29], or stereotypical undetected movements preceding wheel rotations. After about half a second of transient increase,

responses were followed by a delayed suppression (Fig. 1f,g). Also in this case, the overall dynamics could be well summarized in terms of a standing wave of activity (Extended Data Fig. 3a). An analysis of the residuals from the wave dynamics identified a small but significant response in motion-sensitive areas (Extended Data Fig. 3c), likely related to the stimulus motion induced by the wheel rotation (closed-loop period, CL, Fig. 1a).

Inhibitory activity (PV-cre line, n=5) approximately mirrored excitatory activity both for saccades and body-movements[20,30,31]. Responses were ~2.5x and ~2.9x larger than those evoked by visual stimuli[26] (Fig. 1f,g) with an amplitude increase preceding saccadic and body movements (Extended Data Fig. 2c). Both saccades and body movements had a delayed suppression and the overall response in blank conditions resembled those of excitatory neurons (Extended Data Fig. 4a-c). Responses were widespread[32] with a similar cortical localization as excitatory neurons (Fig. 1g). The overall dynamics was also consistent with a standing wave of activity (Extended Data Fig. 3a).

In summary, saccadic and body movement responses were consistent with standing waves of activity and were several folds larger than contrast responses, with spatially distinct activation patterns (Extended Data Fig. 2e,f). Both CDs were characterized by non-sensory components emerging before the movement, and had a delayed suppressive response that could not be fully explained by an overlapping slow intrinsic signal[26,33-35] since it was not observed in response to retinal inputs (Fig. 1f, stimulus and simulated saccades). There was a strong similarity in the spatial and temporal activity patterns of PV and excitatory populations[30], with excitation and inhibition (E-I) seemingly balanced during saccadic and body-movement CDs.

Saccades and body movements often occurred in close temporal proximity and soon after stimulus onset (Fig. 1d, Extended Data Fig. 1b), giving us the opportunity to examine the properties of the stimulus-CD and of the CD-CD interactions. For stimulus-CDs interactions we calculated average responses in trials when saccades or body movements occurred in close temporal proximity with the stimulus onset (Methods). A prominent feature was a significant larger peak response amplitude than for isolated visual responses (Fig. 2a,b; Extended Data Fig. 5a,b). The duration of stimulus-CD response was comparable to that of isolated saccade or body-movement CDs. Moreover, the spatial distribution also resembled that of saccades or body movements (Extended Data Fig. 5c). An analysis of linearity (GLM, Methods) revealed that the saccade and stimulus interaction was supralinear, while the body-movement and stimulus interaction was sub-linear when stimulus and CD coincided, but it was supralinear when the CD followed the stimulus[15] (Extended Data Fig. 6). When saccadic and body movement CDs interacted within short temporal windows, peak response amplitudes were larger than for isolated CDs but significantly smaller than their linear sum (Fig. 2c; Extended Data Fig. 7a-f). We confirmed this was not a result of GCaMP-signal saturation (Extended Data Fig. 7i). Responses also had a strong delayed suppression (Fig. 2c), largest at 2.2±0.2s from the time of interaction. The spatial pattern of the peak CD-CD interaction was mostly a superposition of isolated CDs and it was distinct from the spatial pattern of the delayed suppression, which was more uniformly localized in anterior regions (Extended Data Fig. 7g,h). The sublinear summation was well captured by an overall suppressive component in a GLM-derived interaction kernel (Fig. 2d-g, Methods). Notably, the strongest suppressive interaction occurred when a saccade happened after a body movement (Fig. 2e-f; Extended Data Fig. 8a,c). Similar to the spatial pattern of the peak CD-CD interaction, the nonlinear suppressive component at the time of its maximum was broadly distributed across visual areas, with the peak suppression localized similarly to the isolated saccadic response (Fig. 2g). In PV mice the CD-CD interaction was also suppressive and asymmetric, but less pronounced than for excitation (Extended Data Fig. 8b,d-g). In summary, the contrast response was overshadowed by the

interacting CDs, resulting in a response profile similar to that of CDs in isolation. Interactions were nonlinear, and depended on the lag between stimulus onset and saccade or body movement. The CD-CD interaction was primarily suppressive, with an asymmetry relative to the order of the CDs. Interacting responses were localized in the medial part of V1 and in the medial-anterior dorsal stream areas, being more prominent in excitatory neurons than in PV cells.

Next, we examined how the summation dynamics between CDs and with visual stimuli might affect the processing of visual information and consequently the animal's sensory perception. We started by formulating a simple hypothesis for the previously described temporal asymmetry in the interactions, reasoning that the order of motor execution (saccade or body movement first) could link to learned behavioral patterns in trained mice. For example, a mouse highly engaged in the task could first visually explore (saccade) and then make a wheel movement, with the reverse order being more typical of less engaged animals. Since cognitive-state changes (i.e. task engagement, attention, arousal, etc.) are known to correlate with changes in cortical states[36-39], the asymmetry would emerge because movements with different temporal orders occur in different cortical states. Consistent with this hypothesis, also the processing of CDs in isolation – and of visual signals – should depend on cortical states and correlate with performance, as a reflection of changes in cognitive states. To examine these possibilities we analyzed differences in cognitive states[38] using pupil dilation as a biomarker[38], evaluated visual perception through the animal's ability to discriminate orientations in the 2AFC task, and measured the dynamics of cortical states via quantifiers derived directly from the neural responses.

To characterize the link between cognitive states, performance and cortical states, we pooled across all CD interactions and defined a space of pupil baseline and area change, (Fig. 3a-c, Extended Data Fig. 2h, Methods), associated to tonic and phasic changes in pupil dilations[31,40]. As expected, the animal's performance varied across regions of this pupil space, with gradual increase in performance for larger pupil area (Fig. 3b,c), and with a trend for peak performance at intermediate values of area change (Fig. 3c), in agreement with Yerkes-Dodson inverted U- curve[41]. Notably, correct trials extended to regions of the largest pupil area, more so than incorrect trials, while time-out trials densely clustered in the region of small pupil area, suggesting an overall reduction in task engagement[8] (Fig. 3b). To quantify differences in cortical states, we relied on two measures. First, we defined a dynamical range index (DR) that measures the standard deviation of the neural response throughout a trial (Methods). Large-amplitude CDs could drive high DR values, but CDs were neither consistently sufficient nor necessary for high DR states (Extended Data Fig. 9a, Fig. 3f,g). This index reflected either changes in cortical states following modulations in the animal's cognitive state[36,42] or undetected sensory-motor components. The former interpretation was supported by the wider spread of trials with high DR in the pupil space (Fig. 3c), also accompanied by higher performance (Fig. 3d,e), suggesting increased arousal or engagement in high DR states. Using the stimulus-locked change in the neural response as a second measure of cortical state (Methods), we observed the highest performance in trials with the largest changes (Fig. 3d). Overall, this measure was an informative regressor of the trial choice, with correct, incorrect, and time-out trials characterized by progressively smaller amplitude changes (Fig.3h). This trend was observed also when splitting trials into high and low DR groups, indicating that the neural-to-behavioral correlation was observable on a trial basis and persisted across a broad range of cortical and cognitive states (Fig. 3h). In summary, when analyzing pupil dilation, neural responses and task performance, we observed a significant correlation between psychometric and neurometric parameters with co-variability in cognitive, performance, and cortical states.

As hypothesized, cortical-state changes affected visual responses and CDs, both when considered in isolation or as interacting. The amplitude of the stimulus-evoked response in isolation from other movements (Methods), was larger and had a higher signal-to-noise ratio[43] (Methods) in high DR states, when performance was also higher (Fig. 4a,b). Responses to isolated saccadic and body movements remained space-time separable (standing waves) across DR states, with the peak amplitude and the delayed suppression both enhanced in high DR states, in accord with a multiplicative gain modulation[5,6] (Fig. 4c,d; Extended Data Fig. 9). A similar dependence on dynamical range and performance was observed in CD interactions (Fig.4e-g). In particular, the non-linear suppression was smaller in high DR states, suggesting increased functional independence between CDs, with interactions better described as a linear sum of isolated CDs (Fig. 4e). Notably, although the E-I ratio was on average balanced in isolated and interacting CDs (Fig. 4f,g), in trials with high DR the initial part of the response was multiplicatively scaled both for E and I activations, but in the later part, E was further reduced than I, skewing the ratio toward an overall response suppression (Fig. 4f,g). A possible explanation relates to the phasic and tonic changes in pupil area that had multiplicative and subtractive effects on the interacting responses (Fig. 3f,g, quadrants 2,3 and 1,4 respectively). Hence a cortical-state dependent recruitment of the brain circuits involved in the pupil control could underlie the late E-I imbalance[20,31,40,44-47]. Regarding the temporal asymmetry in CD interactions, both dynamical range and performance were significantly larger when saccades happened before body movements than in the reverse order (Fig. 4h,i). This asymmetry was invariant with respect to cortical states and observed on a trial basis, i.e. when grouping trials into high or low DR states (Fig. 4i). Together these considerations support the proposed hypothesis that changes in cognitive state associated to higher performance and larger DR values, better correlate with a behavioral pattern where visual exploration precedes body movements. Further support to this interpretation comes from the observation that saccades after stimulus onset, but not those preceding it, correlated with higher performance (Extended Data Fig. 6e). According to a mechanistic interpretation, the functional circuits recruited by the CDs are differentially modulated by the animal's cognitive state[36-38]. This is possible via cholinergic[48,49] and noradrenergic neuromodulatory systems known to be robustly activated by these CDs and implicated in the control of arousal and attention[50-52] (Fig. 4j). This mechanistic view suggests a simple computational-level interpretation of how CD interactions influence perception. Performance modulation could be causally linked to a cognitive effect (e.g. related to attention, engagement, etc.), to a perceptual one (e.g. related to the processing of visual signals) or to a combination of the two. All our results support the last interpretation. On one hand high DR states correlated with larger pupil dilations, indicative of a cognitive modulation. On the other hand, in high DR states CDs were larger, together with larger amplitude and S/N of the contrast responses. Furthermore, GLM analysis (Fig. 4e) indicates that the nonlinearities are most negligible in high DR states, suggesting a functional independence (orthogonality) between signals in an encoding space of neural activations[53]. Hence, downstream networks can better decode and use CDs-related information (e.g. for perceptual stabilization[13,54,55] and predictive coding[3,19]) when CDs and visual signals are linearly and independently combined. This interpretation also agrees with findings that during saccades visual information is not necessarily gated away, but rather it is retrievable depending on the visual stimulus and task structure[56]. In conclusion, these results reveal a cognitive and cortical-state dependent arithmetic for the interaction of signals that overshadow sensory activations in sensory cortices, introducing a novel experimental and computational framework for the study of visual perception in ethological conditions.

Methods

Animals

Transgenic mice used in this work were Thy1-GCaMP6f mice (n=10, "excitatory mice"), and PV-Cre mice injected with AAV9-CAG-FLEX-GCaMP6f (n=5, "PV mice"). A large proportion of the PV cell population was successfully driven to express GCaMP6f (Fig. 1e, Extended Data Fig. 1c). When inclusion criteria reduced the number of animals used for specific analysis, we indicated the number accordingly. For all reported results, the number of sessions per animal ranged from 9 to 60, with a minimum and maximum number of trials per animal from 1000 to 8000.

Behavioral training

Animals were trained in a 2AFC orientation discrimination task. Two oriented Gabor patches (20° static sinusoidal gratings, sf = 0.08 cpd, randomized spatial phase, 2D Gaussian window, sigma=0.25°) were shown on the left and right sides of a screen (LCD monitor 25 cm distance from the animal, 33.6 cm × 59.8 cm [~68° × 100°dva], 1920 × 1080 pixels, PROLITE B2776HDS-B1, IIYAMA) at ±35° eccentricity relative to the body's midline. Mice had to report which of the two stimuli matched a target orientation (vertical, n=12; horizontal, n=3). The smallest orientation difference varied depending on animals, from 3° to 30°. Animals made the choice by rotating a rubber wheel with their front paws (Fig.1a; Supplementary video 2), which shifted stimuli horizontally on the screen[21,23]. For a response to be correct, the target stimulus had to be shifted to the center of the screen, upon which the animal was rewarded with 4μL of water. Incorrect responses were discouraged with a prolonged (10s) inter-trial interval and a flickering checkerboard stimulus (2Hz). If no response was made within 10 seconds (time-out trials), no reward nor discouragement was given.

Animals were imaged after exceeding a performance threshold of 75% correct rate for 5-10 consecutive sessions (typically after ~4-12 weeks) when trained in the automated self-head-restraining setups. Depending on animals, performance in the imaging setup (e.g. Fig. 1b) could fluctuate from session to session. To work with a coherent behavioral dataset, we excluded sessions with exceedingly large fractions of time-outs (>=20%) or with average performance below 60%.

Every trial consisted of an open-loop period (OL: 1.5s) and a closed-loop period (CL: 0—10s), followed by an inter-trial interval (ITI: 3—5s). We recorded cortical responses, wheel rotations and eye/pupil videos from a pre-stimulus period (1s duration). Stimuli were presented in the OL period, when wheel rotations did not produce any stimulus movement. In 25% of the trials, the OL lasted longer by an additional randomized 0.5—1.5s period during which we presented simulated-saccade stimuli: i.e. patches moving passively on the screen according to the previously recorded eye movement velocities (Extended Data Fig. 1d).

The psychometric curve

We fitted the animal's probability of making a right-side choice as a function of task difficulty using a psychometric function[57] $\psi(\epsilon;\ \alpha,\beta,\gamma,\lambda) = \gamma + (1-\gamma-\lambda)\,F(\epsilon;\alpha,\beta)$, where $F(x)$ is a Gaussian cumulative probability function, α and β are the mean and standard deviation, γ and λ are left and right (L/R) lapse rates, ϵ is the signed trial difficulty. Confidence intervals were computed by bootstrapping (n=999).

Detection of saccades and body movements

Eye tracking

We monitored the left, contralateral eye illuminated by IR LED (SLS-0208-B medium Beam, Mightex®), using a CMOS camera (FL3-U3-13E4M-C, POINT GREY) equipped with a zoom lens (Navitar Zoom 7000, 1280x1024 pixels, typical ROI size: 350x250 pixels, 30Hz acquisition rate) with an IR filter (Kenko PRO1D R72, 52mm). The camera was aligned to the perpendicular bisector of the eye, making ~60° angle with the midsagittal axis of the animal.

Automatic tracking of the pupil position was done with custom software (Matlab toolbox, G*itHub Link*). We first processed each video frame to extract the visible region of the eye ball (Extended Data Fig. 10a, MATLAB imreconstruct.m and factorization-based texture segmentation[58]), with morphological operations (dilation, erosion, disk structuring elements 106 and 202µm, respectively) to remove pixel noise (Extended Data Fig. 10a). To extract the pupil segment, which has lower intensity values, we performed Otsu thresholding[59] on the intensity distribution in every frame (Extended Data Fig. 10b). We further imposed geometrical constraints to reduce misclassification of the pupil with the eyelid shadows: the pupil had to: 1) be closer to the center of eye segment (Euclidean distance); 2) have a roundness index (4*pi*area/perimeter^2) >0.7. We fitted an ellipse to extract the pupil center position and area, then used for saccade-detection and pupil area analyses. We also confirmed accuracy of pupil-tracking by visually inspecting hundreds of trials.

Saccade Detection

To detect saccadic eye movements, we first filtered the XY positions of the pupil center over time (frames) using an edge filter [-1 -1 0 1 1] and transformed the resulting time series to XY velocities, then we applied an adaptive elliptic thresholding algorithm to find the saccade time-frames that had velocities larger than the elliptic threshold[60] (Extended Data Fig. 10c). We discarded the saccades that lasted <=60ms and were smaller than 1.5° (see ERA method-section for the robustness of the results relative to specific threshold values). We extracted the time, magnitude, duration, velocity, start and landing positions of each saccade (Fig. 1c,d).

Pupil Area

To analyze the pupil area (Fig.3a) we first converted eye-tracking-camera pixels to mm using direct measurements of the width and length of the eye to account for experiment-to-experiment variability in the zooming factor. We calculated the average pupil area for each imaging session by averaging area values across all trials within the session. Finally, pupil area in every trial was normalized (subtracted) relative to the session mean.

Wheel detection

To automatically detect the time at which the animals rotated the wheel, we first converted the wheel rotation values into velocities and flagged as potential wheel movements the time-bins when the velocity had a zero-crossing (i.e. sign change) or deviated from zero above a fixed threshold (20°). All movements smaller than such threshold were considered unintentional twitches of the wheel and discarded (see ERA method-section for the robustness of the results relative to specific threshold values).

Imaging

Expert mice were placed under a macroscope for wide-field imaging (THT, Brain Vision) using a head-plate latching system[21]. The macroscope was equipped with a CMOS camera (pco.edge5.5, pixel size: 6.5µm^2, pixel number: 5.5mp) and two lenses (NIKKOR, 50mm, F1.2, NA = 0.46) to image GCaMP6f fluorescent signals: excitation light, 465nm LED (LEX2B, Brain Vision); emission filter, band-pass at 525±25nm (Edmund).

Retinotopy

We computed maps of retinotopy to identify primary and higher visual areas. Briefly, we used a standard frequency-based method with slowly moving horizontal and vertical flickering bars in anesthetized mice (~0.8% Isoflurane) on a 40" LCD monitor (Iiyama®). Visual area segmentation (Fig. 1e and Extended Data Fig. 1c), was done based on azimuth and elevation gradient inversions as detailed elsewhere[61-63]. To center and orient maps across animals we used the centroid of V1 and the iso-azimuth line passing through it[61].

Pre-processing Wide-field GCaMP6f signals

We first motion corrected GCaMP data[64]. Using a semi-automated control-point selection method (MATLAB cpselect, using blood vessel images), all image frames were registered to a previously acquired retinotopic map. To compute relative fluorescence responses, we calculated a grand-average scalar ${F_0}^{i,j} =< I^{i,j}_{x,y,t} >_{x,y,t}$, with $I^{i,j}_{x,y,t}$ the XYT image tensor in trial *i*, session *j*. We then used this scalar to normalize the raw data tensor $F^{i,j}_{x,y,t} = (I^{i,j}_{x,y,t} - {F_0}^{i,j})/{F_0}^{i,j}$. Data in each trials was then band-pass filtered ([0.1 12] Hz) and smoothed with mild spatial filtering (Gaussian σ = 20μm). Finally, each tensor was compressed with spatial binning (130x130μm^2 with 50% overlap). The results presented do not critically depend on any of these parameters.

Data Analysis

Event Related Analyses (ERA)

We analyzed isolated events in windows that contained only one of the four events: stimulus, simulated saccade, saccade and body movements (Fig.1f, Extended Data Fig. 10d,e). The stimulus isolation window was from 1s before to 1s after the stimulus onset; the simulated saccades window was from trial start to 3s after stimulus onset; the saccades and body movement window, from 2.5s before to 2.5s after the event (Extended Data Fig. 10d). The window sizes were chosen by considering the time needed for the response to return to baseline during a quiescence period (Extended Data Fig. 10h,i). For interacting saccade and body movements, we selected trials with body movement within time-lag windows of [-0.75, -0.25]s, [-0.25, 0.25]s and [0.25, 0.75]s around a saccade (or vice versa). We also excluded trials when other events were detected 2.5s away from the closest event on each side, see the isolation window and event distributions in Extended Data Fig. 10f,g for lag -0.25—0.25s.

For event-related analysis (ERA) we computed trial-averaged responses centered on the time of the event. Spatially, we defined 4 ROIs for each event: we first identified the time of peak response amplitude in V1 and then selected pixels above a varying threshold, from 70th to 99th percentile at steps of 0.5 percentiles, to create binary mask-images. We then averaged the masks (Extended Data Fig. 10j-m) and defined an ROI as a contiguous group of pixels above the 99th percentile (Extended Data Fig. 10n). The results presented did not critically depend on any of the parameters above. Temporal event-related responses in each ROI were computed as a within ROI pixel average after frame-0 correction. This was done by computing an average dF/F in a time window [-0.2 0s] from stimulus onset and simulated saccade, or [-0.8 -0.3s] from saccade and body movements, averaged across trials and animals, and subtracting this value from the event-related responses. Error bars in across-animal averages are always standard error of the mean (s.e.) while across-trial error bars are always 95% confidence interval (95% CI). Peak responses were computed by averaging within a 100ms window centered at the time of max amplitude. To compute spatial maps (Fig. 1g, and most maps in Extended Data Figures), we normalized (z-scored) the dF/F of each pixel in every frame with max amplitude over time: $Z = \frac{\langle F_i \rangle}{k+\sigma(F)_i}$ where F_i is the peak amplitude (average of peak frame ±1 frame) on trial i, $\langle F_i \rangle$ is the average across trials, σ is the standard deviation across trials, and *k* is a small regularizing scalar to avoid division by zero. Then we averaged z-scored responses across mice (Fig. 1g). This was done for both data and the SVD model (singular value decomposition). For SVD analyses (Extended Data Fig. 2), we modeled spatial-temporal response tensors (D) using the SVD components with the highest variance explained, i.e. as a matrix multiplication of a temporal vector (T) with a 2D image component (S), plus residuals (R): $\mathrm{D} = \alpha\ (\mathrm{S\ x\ T}) + \mathrm{R}$, with α a scaling factor. Variance explained was computed as in Geisler et al[65].

Saccadic and body movement velocities below the detection threshold could modulate the amplitude of the isolated saccadic response (Extended Data Fig. 2i-j). We quantified this in trials with isolated saccades, normalizing saccadic and wheel movement velocities by their trial-average maximum. For every trial, we calculated the average velocity within a [-0.5, +1]s time window centered on the time

of the saccade. We then divided trials into small and large wheel velocity groups using the mean velocity across all trials as a threshold. This small contamination of below-threshold velocities did not depend on whether the movement occurred in isolation or together with other movements (Extended Data Fig. 9a).

Linear prediction with jittered times

To compute the linear prediction for stimulus-CD interactions (Fig. 2a,b), we convolved the isolated CD responses (Fig. 1f) with binary input vectors representing recorded movement times, summed them with the isolated stimulus response, and averaged across trials and animals. Similarly, for CD-CD interactions (Fig. 2c), we convolved the responses to isolated body movements and saccades with the corresponding binary input vectors, aligned them to the time of saccade, and averaged across trials.

Signal Saturation

For a given trial i with a pair of saccade and body movement events with a time lag of [-0.25, 0.25]s we calculated a baseline fluorescence image F_0^i by averaging raw fluorescence values over t = [-0.8, 0]s. We also calculated a peak fluorescence image F^i by averaging frames over a 100ms window centered at the time of peak response. Percentage amplitude change was defined as $\delta^i = \frac{F^i - F_0^i}{F_0^i} * 100$. Then, we divided the distribution of F_0^i derived from all trials into 5 equal amplitude intervals (quintiles), and for each interval computed mean F_0^{bin} values together with corresponding mean percentage changes δ^{bin}. For every animal we plotted δ^{bin} as a function of F_0^{bin} with its 95% CI (Extended Data Fig. 7i). We discarded intervals with less than 25 trials.

Pupil and Neural Space, and DR

In pupil space the x-axis was the baseline pupil area, i.e. the average area in the [0, 200] ms interval after the stimulus onset, and the y-axis was the maximum area change relative to this baseline in the OL period (Fig. 3b). For interacting events (Fig. 3f), the baseline was the pupil area at the time of first event (±50ms) and the maximum change was calculated in a [0, 4] interval after the second event (Fig. 3f). A similar procedure was used to define the dF/F neural space (Fig. 3d,h). The dynamical range index (DR) was calculated using the standard deviation of the V1 response over the whole trial duration $DR_i = \sigma(R_{i,t})$ where R is the V1 response in trial i over time t. Calculating DR values including responses from other areas did not significantly change these results. To define 'high' and 'low' DR states we used 75th and 25th percentiles of DR distribution across all trials.

Data used in GLM

In each trial, for every pixel, GCaMP responses were frame-zero corrected by subtracting the average dF/F in the [-1.0, -0.8]s interval before stimulus onset. Data was down-sampled to 10 Hz, and spatially binned: 300x300µm pixel size, "tile" in the following. Only responses in the open loop were analyzed to exclude activations due to stimulus motion. Trials with events in the [-1.0, -0.8]s interval before stimulus onset, or with blinks or simulated saccades were excluded.

Model

For a given tile and trial, we model the GCaMP response $\boldsymbol{y}(\boldsymbol{t})$ as $\boldsymbol{y} = \sum_{i=1}^{I} \boldsymbol{w}_i * \boldsymbol{x}_i + \boldsymbol{\varepsilon}$, with convolutional kernels $\boldsymbol{w}_i$, Gaussian noise $\boldsymbol{\varepsilon} \sim N(0, \boldsymbol{\Sigma})$, and inputs $\boldsymbol{x}_i$, $i \in \{s, b, e, sb, se, be\}$, with s, b, e, stimulus onset, body movement, eye movements, and their pairwise combinations, sb, se, be. Each $\boldsymbol{x}_i$ was a binary time series, with 1's at the time of an event. Pairwise inputs were the outer product of corresponding linear inputs. Kernels $\boldsymbol{w_i}$ acted causally and anticausally to account for both pre- and post-movement responses. The bias term was zero since $\boldsymbol{y}$ was frame-zero corrected.

Optimization

In matrix form $\mathbf{Y} = \mathbf{X}\mathbf{w} + \boldsymbol{\varepsilon}\mathbf{I}$; we estimated kernels from 40 data bootstraps using ridge regression, $\widehat{\boldsymbol{w}} = (\boldsymbol{X}^T\boldsymbol{X} + \boldsymbol{\varepsilon}\boldsymbol{I})^{-1}\boldsymbol{X}\boldsymbol{Y}$, where the optimal ε is found for every tile and kernel $\boldsymbol{w}_i$ by maximizing log marginal likelihood using a fixed-point algorithm[66,67]. The expression for $\widehat{\boldsymbol{w}}$ is equivalent to Bayesian MAP estimate with $\varepsilon = \sigma_n^2/\sigma_p^2$, where σ_n^2 is noise variance of observations and σ_p^2 is prior variance[68]. $\widehat{\boldsymbol{w}}$ is biased, with the amplitude of kernels estimated from relatively few noisy trials strongly penalized (e.g. Extended Data Fig. 8.g, right).

Sequential fitting

To eliminate the trade-off between kernels of different inputs, we estimated them sequentially[69]. We estimated $\boldsymbol{w}_s$ from trials with no body or eye movements until 2.8s after trial start, $\boldsymbol{w}_s$ was estimated in a time window τ_s = (-1.0s, 1.5s) centered on the stimulus onset and could also contain a slow upward/downward trend related to movements in the ITI period. From the residuals, $\boldsymbol{y}_{rs} = \boldsymbol{y} - \boldsymbol{w}_s * \boldsymbol{x}_s$, we estimated $\boldsymbol{w}_e$, with τ_e = (-0.3s, 2.0s) and $\boldsymbol{w}_b$ with τ_b = (-0.3s, 2.0s) using segments of trials where the movements were isolated. Isolation meant no overlap with any part of the τ-window of any surrounding movements. From the residuals, $\boldsymbol{y}_{rsbe} = \boldsymbol{y}_{rs} - \boldsymbol{w}_b * \boldsymbol{x}_b - \boldsymbol{w}_e * \boldsymbol{x}_e$, we estimated the body-eye movement interaction kernel $\boldsymbol{w}_{be}$, τ_{be} = [(-0.3s, 2.0s), (-0.3s, 2.0s)] using all trials. Finally, we estimated stimulus-eye movement $\boldsymbol{w}_{se}$ (using dF/F downsampled at 5Hz) and stimulus-body movement $\boldsymbol{w}_{sb}$ kernels from the residuals $\boldsymbol{y}_{rse} = \boldsymbol{y}_{rs} - \boldsymbol{w}_e * \boldsymbol{x}_e$ and $\boldsymbol{y}_{rsb} = \boldsymbol{y}_{rs} - \boldsymbol{w}_b * \boldsymbol{x}_b$, using the same trial segments as when fitting $\boldsymbol{w}_e$ and $\boldsymbol{w}_b$ respectively to ensure isolation.

Kernel analysis and figures

Used data

Due to the stringent trial-selection criteria, $\boldsymbol{w}_{be}$ could be reliably estimated from n=8 excitatory animals and n=5 PV animals; $\boldsymbol{w}_{se}$ from n=5 excitatory animals, $\boldsymbol{w}_{sb}$ from n=6 excitatory animals. $\boldsymbol{w}_{se}$ and $\boldsymbol{w}_{sb}$ could be estimated in fewer excitatory animals than $\boldsymbol{w}_{be}$ because we additionally required isolation of the respective movement. $\boldsymbol{w}_{se}$ and $\boldsymbol{w}_{sb}$ could not be reliably estimated for PV animals.

Graphical representation and pre-processing

We represent kernels $\boldsymbol{w}_{be}$, $\boldsymbol{w}_{se}$, $\boldsymbol{w}_{sb}$ in the coordinates of lags, (τ_b, τ_e), (τ_s, τ_e), (τ_s, τ_b) - (Fig. 2e; Extended Data Fig. 6b,d; Extended Data Fig. 8a,b), a kernel element is thus e.g. $w_{be}(\tau_b, \tau_e)$. For improved graphics, we filtered $\boldsymbol{w}_{be}$, $\boldsymbol{w}_{se}$, $\boldsymbol{w}_{sb}$ in the lag-lag space with a mean filter of 3x3 time bins. For the results presented, we only considered elements significantly different from zero (two-tailed Mann-Whitney U-test at $\alpha = 0.05$), that passed the permutation test ($\boldsymbol{w}_{be}$ only), and that could be estimated from at least 10 data points – these criteria were tested for all animals, all tiles, and lags. Permutation test for $\boldsymbol{w}_{be}$ was performed by randomly assigning trials with interactions to saccade-body movement pairs with different $\Delta\tau$ and fitting the GLM with ε fixed at the unshuffled estimate. $\boldsymbol{w}_{be}$ was then tested against the shuffled-data estimate of $\boldsymbol{w}_{be}$ using Mann-Whitney U-test (α=0.05).

Population kernels

We calculated population kernels $\boldsymbol{w}_{be}^{pop}$, $\boldsymbol{w}_{se}^{pop}$, or $\boldsymbol{w}_{sb}^{pop}$ (Fig. 2e; Extended Data Fig. 6b,e; Extended Data Fig. 8a,b), as average normalized kernels $\boldsymbol{w}_{be}$, $\boldsymbol{w}_{se}$, $\boldsymbol{w}_{sb}$ belonging to the tiles (300x300µm) with the most suppressive $w_{be}(\tau_b, \tau_e)$ and $w_{sb}(\tau_s, \tau_b)$ or most facilitating $w_{se}(\tau_s, \tau_e)$ values. The patterns of suppression and facilitation of $\boldsymbol{w}_{be}$, $\boldsymbol{w}_{se}$, $\boldsymbol{w}_{sb}$ did not change substantially as we considered different larger regions (data not shown). We masked elements $\boldsymbol{w}_{be}^{pop}$ (dim colors) that were indistinguishable from permutated data or could not be estimated in n=3 or more (of 8 total) animals (in n=2 or more (of 5) for PV animals). We masked elements $\boldsymbol{w}_{se}^{pop}$ and $\boldsymbol{w}_{sb}^{pop}$ if they could not be estimated in n=2 or more (of 6) animals.

We show (τ_b, τ_e) of maximally suppressive elements of every animal with a red dot, and population average $\langle(\tau_b, \tau_e)\rangle$ – with a red circle (Fig. 2e), s.e. smaller than circle size. We excluded one outlier

mouse. Similarly, we show maximally facilitating $w_{se}(\tau_s, \tau_e)$ of individual animals with black asterisks and mean±s.e. as a circle with error bars (Extended Data Fig. 6e). We show maximally suppressive $w_{sb}(\tau_s, \tau_b)$ with black circles, maximally facilitating $w_{sb}(\tau_s, \tau_b)$ as black crosses, and respective population medians and median-based standard errors as a large circle and a large cross (Extended Data Fig. 6b). Markers of all animals were jittered with Gaussian noise of $\sigma = 0.1$ to avoid overlap in the graphics.

GLM simulated responses

We predicted nonlinear components of the response using the GLM (Fig. 2g; Extended Data Fig. 6c,f; Extended Data Fig. 8c,d), where all but the corresponding nonlinear term was set to zero. Responses were generated according to lags highlighted on the respective population kernels.

Maximum suppression at relative lag and time

From normalized kernels of individual mice, we found maximum suppression as a function of relative lag $\Delta\tau_{be}$, $\Delta\tau_{sb}$, $\Delta\tau_{se}$ and time Δt_{be}, Δt_{sb}, Δt_{se} (Fig. 2f; Extended Data Fig. 6g-l; Extended Data Fig. 8e,f), computed an average curve, and compared population values at all lags with those at the lag of the minimum of the average curve (Fig. 2f; Extended Data Fig. 6k,l; Extended Data Fig. 8e,f; U-test, α=0.05) or at the lag of the maximum of the average curve (Extended Data Fig. 6g-j), and marked significantly different $\Delta\tau$ and Δt with asterisks. We additionally report the mean of $\Delta\tau_{min}$ and Δt_{min} across animals, i.e. the average abscissa of the minima (Fig. 2f; Extended Data Fig. 8e,f).

Explained variance

We estimated response variance of every tile of every animal explained by a full GLM using $R^2 = 1 - \sum_i(\hat{y}_i - y_i)^2 \,/\, \sum_i(y_i - \bar{y})^2$, where $\hat{y}$ is GLM prediction and $\bar{y}$ is data average, with summation done over individual time bins and trials, following a 5-fold cross-validation procedure. We report population average maps of explained variance in percent units (Extended Data Fig. 8g).

Statistics

We use the term 'Wilcoxon' to refer to the Wilcoxon signed-rank test, and 'U-test' to refer to the Wilcoxon rank-sum test. We use confidence intervals of the mean (CI) for within animal confidence statistics. We use standard error of the mean (s.e.) for across animals error estimates. We use t-test to compare mean amplitudes from within-animal data. When pooling maps across animals we first z-score and then average.

References

1 Sommer, M. A. & Wurtz, R. H. Brain circuits for the internal monitoring of movements. *Annual review of neuroscience* **31**, 317-338, doi:10.1146/annurev.neuro.31.060407.125627 (2008).

2 Crapse, T. B. & Sommer, M. A. Corollary discharge across the animal kingdom. *Nature reviews. Neuroscience* **9**, 587-600 (2008).

3 Straka, H., Simmers, J. & Chagnaud, B. P. A New Perspective on Predictive Motor Signaling. *Current biology : CB* **28**, R232-R243, doi:10.1016/j.cub.2018.01.033 (2018).

4 Sommer, M. A. & Wurtz, R. H. A pathway in primate brain for internal monitoring of movements. *Science* **296**, 1480-1482 (2002).

5 Dadarlat, M. C. & Stryker, M. P. Locomotion Enhances Neural Encoding of Visual Stimuli in Mouse V1. *The Journal of neuroscience : the official journal of the Society for Neuroscience* **37**, 3764-3775, doi:10.1523/JNEUROSCI.2728-16.2017 (2017).

6 Mineault, P. J., Tring, E., Trachtenberg, J. T. & Ringach, D. L. Enhanced Spatial Resolution During Locomotion and Heightened Attention in Mouse Primary Visual Cortex. *The Journal of neuroscience : the official journal of the Society for Neuroscience* **36**, 6382-6392, doi:10.1523/JNEUROSCI.0430-16.2016 (2016).

7 Busse, L. *et al.* Sensation during Active Behaviors. *The Journal of neuroscience : the official journal of the Society for Neuroscience* **37**, 10826-10834, doi:10.1523/JNEUROSCI.1828-17.2017 (2017).

8 Vinck, M., Batista-Brito, R., Knoblich, U. & Cardin, J. A. Arousal and locomotion make distinct contributions to cortical activity patterns and visual encoding. *Neuron* **86**, 740-754, doi:10.1016/j.neuron.2015.03.028 (2015).

9 Burr, D. Eye movements: keeping vision stable. *Current biology : CB* **14**, R195-197 (2004).

10 Cavanaugh, J., Berman, R. A., Joiner, W. M. & Wurtz, R. H. Saccadic Corollary Discharge Underlies Stable Visual Perception. *The Journal of neuroscience : the official journal of the Society for Neuroscience* **36**, 31-42, doi:10.1523/JNEUROSCI.2054-15.2016 (2016).

11 Ibbotson, M. & Krekelberg, B. Visual perception and saccadic eye movements. *Current opinion in neurobiology* **21**, 553-558, doi:10.1016/j.conb.2011.05.012 (2011).

12 McFarland, J. M., Bondy, A. G., Saunders, R. C., Cumming, B. G. & Butts, D. A. Saccadic modulation of stimulus processing in primary visual cortex. *Nature communications* **6**, 8110, doi:10.1038/ncomms9110 (2015).

13 Ross, J., Morrone, M. C., Goldberg, M. E. & Burr, D. C. Changes in visual perception at the time of saccades. *Trends in neurosciences* **24**, 113-121 (2001).

14 Wurtz, R. H., Joiner, W. M. & Berman, R. A. Neuronal mechanisms for visual stability: progress and problems. *Philos Trans R Soc Lond B Biol Sci* **366**, 492-503, doi:10.1098/rstb.2010.0186 (2011).

15 Niell, C. M. & Stryker, M. P. Modulation of Visual Responses by Behavioral State in Mouse Visual Cortex. *Neuron* **65**, 472-479 (2010).

16 Schneider, D. M., Nelson, A. & Mooney, R. A synaptic and circuit basis for corollary discharge in the auditory cortex. *Nature* **513**, 189 (2014).

17 Ayaz, A., Saleem, A. B., Scholvinck, M. L. & Carandini, M. Locomotion controls spatial integration in mouse visual cortex. *Current biology : CB* **23**, 890-894, doi:10.1016/j.cub.2013.04.012 (2013).

18 Leinweber, M., Ward, D. R., Sobczak, J. M., Attinger, A. & Keller, G. B. A Sensorimotor Circuit in Mouse Cortex for Visual Flow Predictions. *Neuron* **95**, 1420-1432.e1425, doi:10.1016/j.neuron.2017.08.036 (2017).

19 Keller, G. B., Bonhoeffer, T. & Hubener, M. Sensorimotor mismatch signals in primary visual cortex of the behaving mouse. *Neuron* **74**, 809-815, doi:10.1016/j.neuron.2012.03.040 (2012).

20 Fu, Y. *et al.* A cortical circuit for gain control by behavioral state. *Cell* **156**, 1139-1152, doi:10.1016/j.cell.2014.01.050 (2014).

21 Aoki, R., Tsubota, T., Goya, Y. & Benucci, A. An automated platform for high-throughput mouse behavior and physiology with voluntary head-fixation. *Nature communications* **8**, 1196, doi:10.1038/s41467-017-01371-0 (2017).

22 Sakatani, T. & Isa, T. Quantitative analysis of spontaneous saccade-like rapid eye movements in C57BL/6 mice. *Neuroscience research* **58**, 324-331, doi:10.1016/j.neures.2007.04.003 (2007).

23 Burgess, C. P. *et al.* High-Yield Methods for Accurate Two-Alternative Visual Psychophysics in Head-Fixed Mice. *Cell reports* **20**, 2513-2524, doi:10.1016/j.celrep.2017.08.047 (2017).

24 Ross, J., Burr, D. & Morrone, C. Suppression of the magnocellular pathway during saccades. *Behavioural brain research* **80**, 1-8 (1996).

25 Lyamzin, D. & Benucci, A. The mouse posterior parietal cortex: anatomy and functions. *Neuroscience research* (2018).

26 Wekselblatt, J. B., Flister, E. D., Piscopo, D. M. & Niell, C. M. Large-scale imaging of cortical dynamics during sensory perception and behavior. *Journal of neurophysiology*, jn 01056 02015, doi:10.1152/jn.01056.2015 (2016).

27 Juavinett, A. L. & Callaway, E. M. Pattern and Component Motion Responses in Mouse Visual Cortical Areas. *Current biology : CB*, doi:10.1016/j.cub.2015.05.028 (2015).

28 Troncoso, X. G. *et al.* V1 neurons respond differently to object motion versus motion from eye movements. *Nature communications* **6**, 8114, doi:10.1038/ncomms9114 (2015).

29 Saleem, A. B., Ayaz, A., Jeffery, K. J., Harris, K. D. & Carandini, M. Integration of visual motion and locomotion in mouse visual cortex. *Nature neuroscience*, doi:10.1038/nn.3567 (2013).

30 Dipoppa, M. *et al.* Vision and Locomotion Shape the Interactions between Neuron Types in Mouse Visual Cortex. *Neuron*, doi:10.1016/j.neuron.2018.03.037 (2018).

31 Reimer, J. *et al.* Pupil Fluctuations Track Fast Switching of Cortical States during Quiet Wakefulness. *Neuron* **84**, 355-362, doi:10.1016/j.neuron.2014.09.033 (2014).

32 Haider, B., Hausser, M. & Carandini, M. Inhibition dominates sensory responses in the awake cortex. *Nature* **493**, 97-100, doi:10.1038/nature11665 (2013).

33 Shimaoka, D., Harris, K. D. & Carandini, M. Effects of Arousal on Mouse Sensory Cortex Depend on Modality. *Cell reports* **22**, 3160-3167, doi:10.1016/j.celrep.2018.02.092 (2018).

34 Xiao, D. *et al.* Mapping cortical mesoscopic networks of single spiking cortical or sub-cortical neurons. *eLife* **6**, doi:10.7554/eLife.19976 (2017).

35 Ma, Y. *et al.* Wide-field optical mapping of neural activity and brain haemodynamics: considerations and novel approaches. *Philosophical Transactions of the Royal Society B: Biological Sciences* **371**, 20150360, doi:doi:10.1098/rstb.2015.0360 (2016).

36 Harris, K. D. & Thiele, A. Cortical state and attention. *Nature reviews. Neuroscience* **12**, 509-523, doi:10.1038/nrn3084 (2011).

37 McCormick, D. A., McGinley, M. J. & Salkoff, D. B. Brain state dependent activity in the cortex and thalamus. *Current opinion in neurobiology* **31**, 133-140, doi:10.1016/j.conb.2014.10.003 (2015).

38 McGinley, M. J. *et al.* Waking State: Rapid Variations Modulate Neural and Behavioral Responses. *Neuron* **87**, 1143-1161 (2015).

39 Engel, T. A. *et al.* Selective modulation of cortical state during spatial attention. *Science* **354**, 1140-1144, doi:10.1126/science.aag1420 (2016).

40 Reimer, J. *et al.* Pupil fluctuations track rapid changes in adrenergic and cholinergic activity in cortex. *Nature communications* **7**, 13289, doi:10.1038/ncomms13289 (2016).

41 McGinley, M. J., David, S. V. & McCormick, D. A. Cortical Membrane Potential Signature of Optimal States for Sensory Signal Detection. *Neuron*, doi:10.1016/j.neuron.2015.05.038 (2015).

42 Churchland, M. M. *et al.* Stimulus onset quenches neural variability: a widespread cortical phenomenon. *Nature neuroscience* **13**, 369-378, doi:10.1038/nn.2501 (2010).

43 Bennett, C., Arroyo, S. & Hestrin, S. Subthreshold Mechanisms Underlying State-Dependent Modulation of Visual Responses. *Neuron* **80**, 350-357, doi:10.1016/j.neuron.2013.08.007 (2013).

44 Zhang, S. *et al.* Selective attention. Long-range and local circuits for top-down modulation of visual cortex processing. *Science* **345**, 660-665, doi:10.1126/science.1254126 (2014).

45 Mitchell, J. F., Sundberg, K. A. & Reynolds, J. H. Differential attention-dependent response modulation across cell classes in macaque visual area V4. *Neuron* **55**, 131-141, doi:10.1016/j.neuron.2007.06.018 (2007).

46 Najafi, F., Elsayed, G. F., Pnevmatikakis, E., Cunningham, J. & Churchland, A. K. Inhibitory and excitatory populations in parietal cortex are equally selective for decision outcome in both novices and experts. *bioRxiv*, doi:10.1101/354340 (2018).

47 Weskelblatt, J. B. & Niell, C. M. Distinct functional classes of excitatory neurons in mouse V1 are differentially modulated by learning and task engagement. *bioRxiv*, 533463, doi:10.1101/533463 (2019).

48 Pinto, L. *et al.* Fast modulation of visual perception by basal forebrain cholinergic neurons. *Nature neuroscience*, doi:10.1038/nn.3552 (2013).

49 Disney, A. A., Aoki, C. & Hawken, M. J. Cholinergic suppression of visual responses in primate V1 is mediated by GABAergic inhibition. *Journal of neurophysiology* **108**, 1907-1923, doi:10.1152/jn.00188.2012 (2012).

50 Aston-Jones, G. & Cohen, J. D. An integrative theory of locus coeruleus-norepinephrine function: adaptive gain and optimal performance. *Annual review of neuroscience* **28**, 403-450, doi:10.1146/annurev.neuro.28.061604.135709 (2005).

51 Schriver, B. J., Bagdasarov, S. & Wang, Q. Pupil-linked arousal modulates behavior in rats performing a whisker deflection direction discrimination task. *Journal of neurophysiology* **120**, 1655-1670, doi:10.1152/jn.00290.2018 (2018).

52 Breton-Provencher, V. & Sur, M. Active control of arousal by a locus coeruleus GABAergic circuit. *Nature neuroscience*, doi:10.1038/s41593-018-0305-z (2019).

53 Semedo, J. D., Zandvakili, A., Machens, C. K., Yu, B. M. & Kohn, A. Cortical Areas Interact through a Communication Subspace. *Neuron*, doi:https://doi.org/10.1016/j.neuron.2019.01.026 (2019).

54 Bridgeman, B., Van der Heijden, A. & Velichkovsky, B. M. A theory of visual stability across saccadic eye movements. *Behavioral and Brain Sciences* **17**, 247-258 (1994).

55 Wurtz, R. H. Neuronal mechanisms of visual stability. *Vision research* **48**, 2070-2089, doi:http://dx.doi.org/10.1016/j.visres.2008.03.021 (2008).

56 Binda, P. & Morrone, M. C. Vision During Saccadic Eye Movements. *Annu Rev Vis Sci* **4**, 193-213, doi:10.1146/annurev-vision-091517-034317 (2018).

57 Wichmann, F. A. & Hill, N. J. The psychometric function: I. Fitting, sampling, and goodness of fit. *Perception & psychophysics* **63**, 1293-1313 (2001).

58 Jiangye, Y., Deliang, W. & Cheriyadat, A. M. Factorization-Based Texture Segmentation. *Image Processing, IEEE Transactions on* **24**, 3488-3497, doi:10.1109/TIP.2015.2446948 (2015).

59 Otsu, N. A Threshold Selection Method from Gray-Level Histograms. *IEEE Transactions on Systems, Man, and Cybernetics* **9**, 62-66, doi:10.1109/TSMC.1979.4310076 (1979).

60 Engbert, R. & Mergenthaler, K. Microsaccades are triggered by low retinal image slip. *Proceedings of the National Academy of Sciences of the United States of America* **103**, 7192-7197, doi:10.1073/pnas.0509557103 (2006).

61 Garrett, M. E., Nauhaus, I., Marshel, J. H. & Callaway, E. M. Topography and areal organization of mouse visual cortex. *The Journal of neuroscience : the official journal of the Society for Neuroscience* **34**, 12587-12600, doi:10.1523/JNEUROSCI.1124-14.2014 (2014).

62 Marshel, J. H., Garrett, M. E., Nauhaus, I. & Callaway, E. M. Functional specialization of seven mouse visual cortical areas. *Neuron* **72**, 1040-1054, doi:10.1016/j.neuron.2011.12.004 (2011).

63 Kalatsky, V. A. & Stryker, M. P. New paradigm for optical imaging: temporally encoded maps of intrinsic signal. *Neuron* **38**, 529-545 (2003).

64 Pachitariu, M., Steinmetz, N. A., Kadir, S. N., Carandini, M. & Harris, K. D. in *Advances in Neural Information Processing Systems.* 4448-4456.

65 Geisler, W. S., Albrecht, D. G. & Crane, A. M. Responses of neurons in primary visual cortex to transient changes in local contrast and luminance. *The Journal of neuroscience* **27**, 5063-5067 (2007).

66 Park, M. & Pillow, J. W. Receptive field inference with localized priors. *PLoS computational biology* **7**, e1002219, doi:10.1371/journal.pcbi.1002219 (2011).

67 Tipping, M. E. Sparse Bayesian learning and the relevance vector machine. *Journal of machine learning research* **1**, 211-244 (2001).

68 Williams, C. K. & Rasmussen, C. E. *Gaussian processes for machine learning*. Vol. 2 (MIT Press Cambridge, MA, 2006).

69 Pho, G. N., Goard, M. J., Woodson, J., Crawford, B. & Sur, M. Task-dependent representations of stimulus and choice in mouse parietal cortex. *Nature communications* **9**, 2596, doi:10.1038/s41467-018-05012-y (2018).

Endnotes

Acknowledgments

Yuki Goya, Yuka Iwamoto, and Rie Nishiyama for their support with animal surgeries and behavioral training. Dr. Fujisawa at RIKEN-CBS for sharing the PV-cre line, Dr. Johansen at RIKEN-CBS for the GCaMP virus. This work was funded by RIKEN BSI and RIKEN CBS institutional funding, JSPS grants in aid 26290011 and 17H06037 to AB, Fujitsu collaborative grant.

Author contributions

AB and MA designed the study. MA collected most data and pre-processed it, developed the eye tracking toolbox and analyzed the eye data, did behavioral, ERA and SVD analyses. DL helped collecting data, developed the GLM toolbox, and did all GLM-related analysis. RA developed the general framework for the behavioral paradigm and helped collecting data. AB supervised all aspects of the work. AB MA DL wrote the manuscript.

Competing interests

The authors declare no competing interests

Correspondence and request for material

Should be addressed to AB: andrea@benuccilab.net

Figures

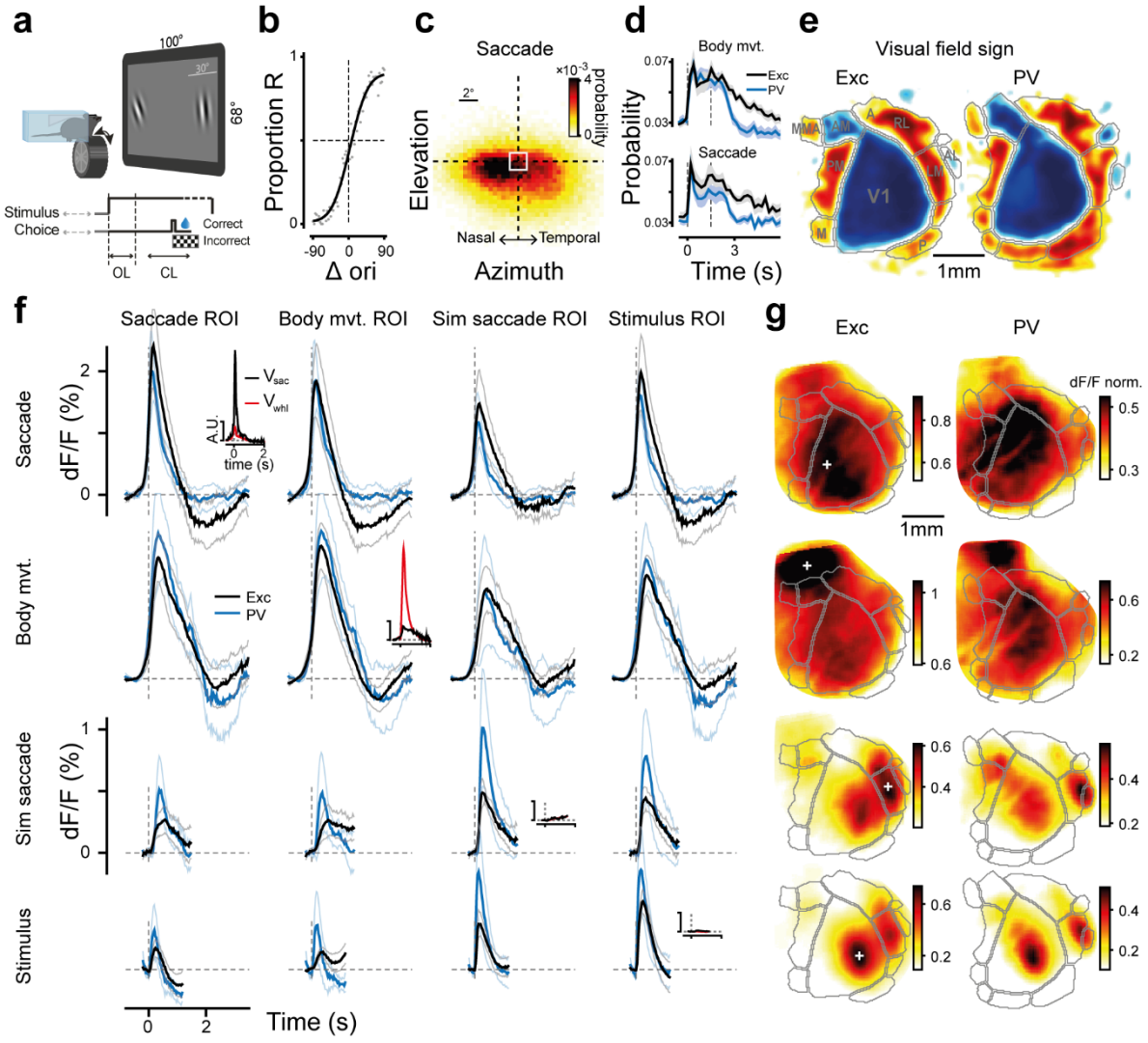

Figure 1. Corollary discharges during decision making. **a**) Setup and task structure. **b**) Psychometric curve, example mouse; black line, fit (Methods); gray dots, data. **c**) Probability of saccade landing positions. White square, session-average eye resting position. **d**) Probability of body movements (top) and saccades (bottom) during the trial, in excitatory (black; n=10) and PV (dark blue; n=5) mice; error bands, s.e. **e**) Visual field sign maps for excitatory and PV mice (n=10 and 5). **f**) Event related responses. Rows 1-4: saccade, wheel, simulated saccade and stimulus, across corresponding ROIs (columns) for excitatory (black) and PV (blue) mice. Max amplitude of saccadic response: 2.5±0.4 (Exc) and 2.1±0.3 (PV), %dF/F ± s.e.; t-test comparing to stimulus response, $p<10^{-4}$. FWHM 0.56±0.06s and 0.46±0.08s (t-test PV vs Exc, p=0.38). Body-movement response: peak 2.2±0.2 and 2.5±0.4; larger than stimulus response, t-test $p<10^{-4}$ and 0.005; FWHM 0.83±0.07s and 0.94±0.11s (t-test p=0.4). Peak simulated saccade response: 0.53±0.04% and 1±0.24%. Peak stimulus response: 0.57±0.05% and 0.9±0.2%. Insets: saccade (black) and body movement (red) velocities for each event, for excitatory mice. **g**) Peak response maps: average normalized responses for each event (rows) at its corresponding peak time, for excitatory (1st column) and PV (2nd column) mice (Methods). Gray area contours as in (e). White crosses indicate ROI centers used in (f), Extended Data Fig. 10 j-n.

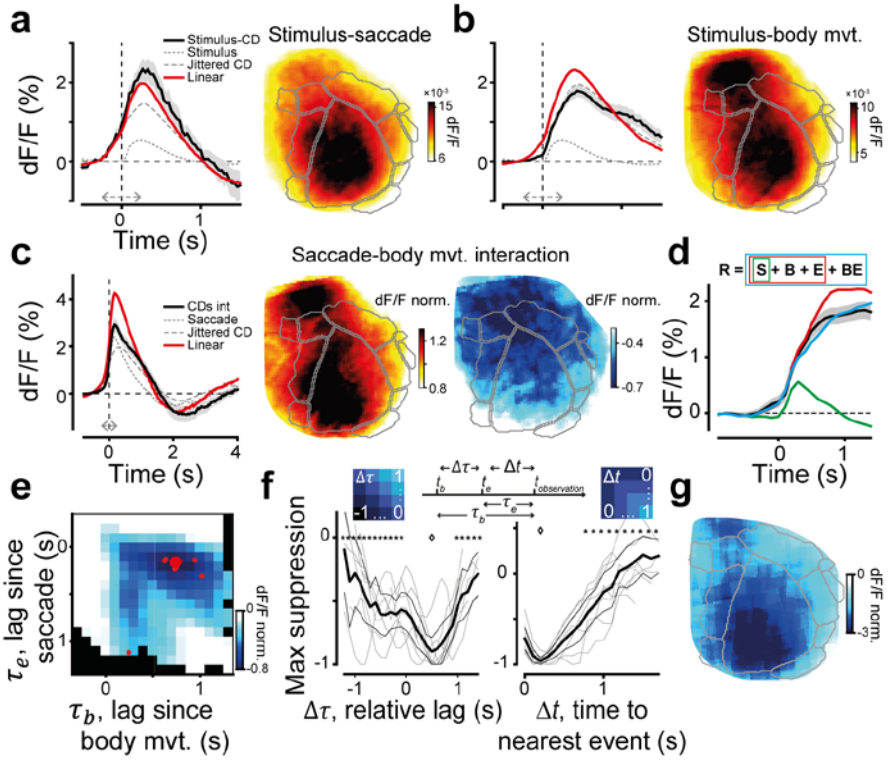

627 Figure 2. Stimulus-CD and CD-CD interactions. **a**) Left: stimulus-saccade interaction for excitation (black) in
628 stimulus ROI and its linear prediction (red), i.e. the sum of stimulus and jittered saccade responses. Horizontal
629 double arrow, jittering window (Methods). Right: spatial map of activation at time of peak response. Peak
630 response amplitude is 3.8x larger than the contrast response (t-test, $p<10^{-4}$; n=10). FWHM: 0.5±0.04s s.e. same
631 as for isolated saccades, t-test p=0.5. **b**) Left: same as in (a), for stimulus-body movement interactions in stimulus
632 ROI. Peak response is 3x larger than contrast response (t-test, $p<10^{-4}$). FWHM: 0.83±0.09s same as for isolated
633 body movements, t-test p=0.98. **c**) Responses to interacting CDs in saccade ROI for excitatory mice. Left: saccade-
634 body movement interaction and linear prediction (red; Methods). Peak responses are 1.2x and 1.3x larger than
635 for isolated saccades and body movements (t-test, p=0.2 and 0.01), but smaller than their linear sum (t-test,
636 $p<10^{-3}$). Middle: spatial response at time of peak amplitude for interacting CDs in excitatory mice. Right:
637 suppressive response at time of peak suppression. **d**) GLM sequential fitting: average dF/F aligned to stimulus
638 onset in trials with CD-CD interactions (black), gray band CI, example mouse. Model responses: stimulus (green),
639 stimulus + isolated CDs (red), stimulus + isolated CDs + nonlinear CD interaction (blue). **e**) Average CD-CD
640 interaction kernel for excitatory mice (n=8) in regions of max suppression (g). Masked black squares if n<5 mice
641 (Methods). Red dots, maximum suppression for individual animals; large circle for population average (lag
642 τ_b=t_{observ}-t_b=0.74±0.06s, τ_e=0.16±0.03s, one outlier omitted, error bars smaller than circle size). **f**) Top center,
643 illustration of relative lag $\Delta\tau = \tau_b - \tau_e$ and time to nearest movement $\Delta t = \min(\tau_e, \tau_b), \tau_e > 0, \tau_b > 0$. Top
644 left and right – schematic of kernel elements with fixed $\Delta\tau$ and Δt, in the same color. Left. Maximum suppression
645 as a function of $\Delta\tau$. Population average, black line (CI, dark gray); individual animals, light gray. Asterisks, values
646 different from minimum of average curve ($\Delta\tau$=0.5, diamond) (U-test, α=0.05). Average $\Delta\tau_{min}$ across animals:
647 0.58±0.05s. Right. Maximum suppression as a function of Δt, same colors as (f). Average Δt_{min} across animals,
648 0.16±0.03s. **g**) Spatial distribution of nonlinear CD-CD component at time of maximum suppression (red circle in
649 (e)).

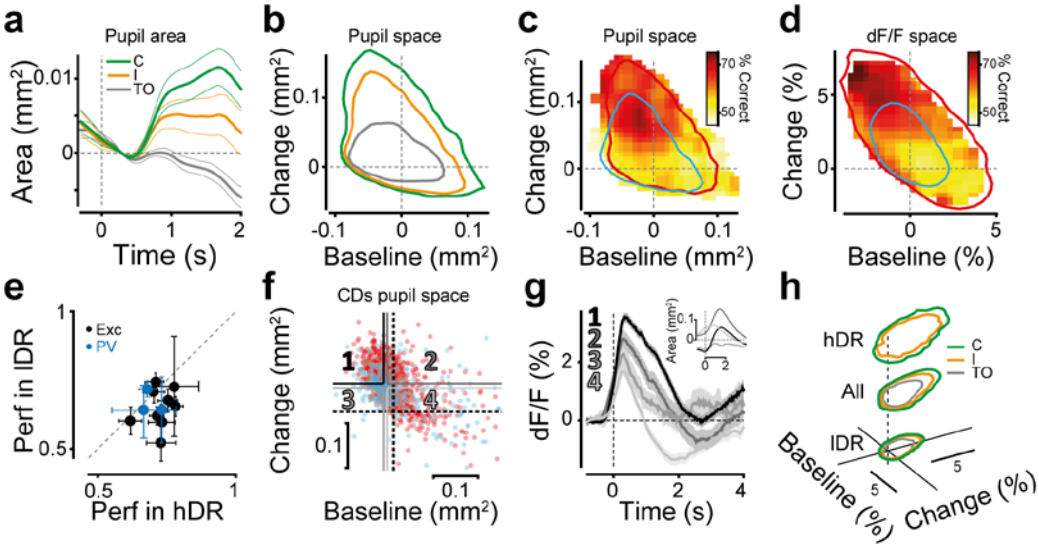

Figure 3. Correlations between pupil dilation, performance and cortical states. **a**) Pupil area changes after stimulus onset for correct (C), incorrect (I) and timeout (TO) choices. **b**) Iso-contour lines (10th percentile) of C/I/TO trial distributions in pupil space (Methods). **c**) Performance in different regions of pupil space. Contour lines (10th percentile) for trials with high (red) and low (cyan) DR. **d**) Performance in different regions of dF/F space (Methods). Contour lines for high and low DR (10th percentile). **e**) Performance in high vs low DR trials (population average for sessions with >60% C and <20% TO, 72±1% correct in high DR; 65±2% in low DR, s.e., difference of the means across animals, p=0.02, Wilcoxon, n=12). **f**) Pupil dilations for interacting CDs. Red and blue dots, high and low DR. **g**) Neural responses for quadrants 1-4 in the pupil space (f). Inset: pupil modulation for the 4 quadrants in (f). **h**) 95th percentile contour lines of C/I/TO distributions in the dF/F space (d), for high, average, and low DR conditions.

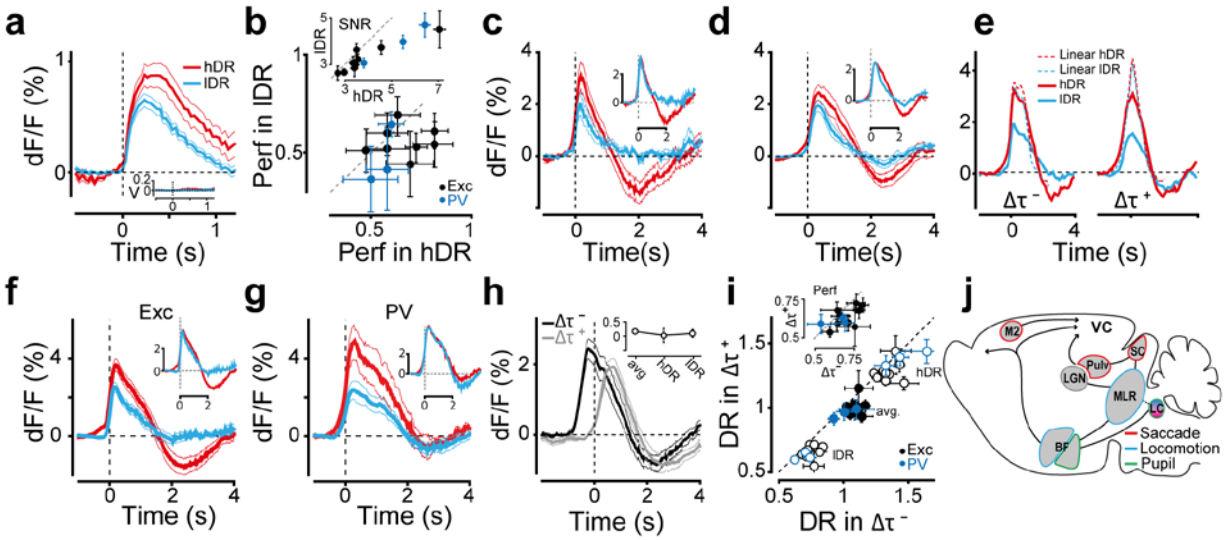

660 Figure 4. DR-dependent modulation of stimulus and CDs. **a**) Responses to isolated stimulus in high (red) and low
661 (blue) DR for excitatory mice. Inset: velocities of saccade and body movements for corresponding conditions. **b**)
662 Performance in high and low DR for trials with isolated stimuli (Wilcoxon p = 0.04, n=11). Only sessions with
663 >50% performance and <30% timeout rate are included. Inset: signal to noise ratio for corresponding trials
664 (Wilcoxon p=0.001). **c**) Responses to isolated saccades in high and low DR. Inset, responses normalized to
665 high/low peak ratio. **d**) Responses to isolated body movements in high and low DR. Inset as in (c). **e**) Left: average
666 dF/F during interactions with relative lags $\Delta\tau^{-}$: -700ms<$\Delta\tau$<-300ms (saccade before body movement, Fig. 2f) in
667 high and low DR. Dotted lines show predictions of the linear part of the GLM, red box Fig. 2d. Right: same as left,
668 but with relative lags $\Delta\tau^{+}$: 300<$\Delta\tau$<700ms (saccade after body movement). Responses are aligned to the time
669 of saccade. **f**) Responses to interacting CDs in high and low DR. Inset, as in (c). **g**) Same as (f) for PV mice. **h**)
670 Response to interacting CDs at different lags, aligned to saccade time. Inset, fractional ratio of $\Delta\tau^{-}$ and $\Delta\tau^{+}$
671 responses averaged across all trials ("avg." label), and in high and low DR. **i**) DR in $\Delta\tau^{-}$ is larger than in $\Delta\tau^{+}$ in
672 hDR, on average, and in lDR conditions (Wilcoxon on means across all trials: all DR p = 0.002, h-DR p = 0.02, l-DR
673 $p<10^{-4}$; and $p<10^{-4}$ for session means in each condition). Inset: average performance in $\Delta\tau^{-}$ versus $\Delta\tau^{+}$
674 (Wilcoxon p=0.007 across all trials). **j**) Schematic of the circuits controlling saccades, body movements, and pupil-
675 related arousal states: VC, visual cortex. Pulv, pulvinar. SC, superior colliculus. LGN, lateral geniculate nucleus.
676 MLR, mesencephalic locomotor region. LC, locus coeruleus. BF, Basal forebrain. M2, secondary motor cortex.